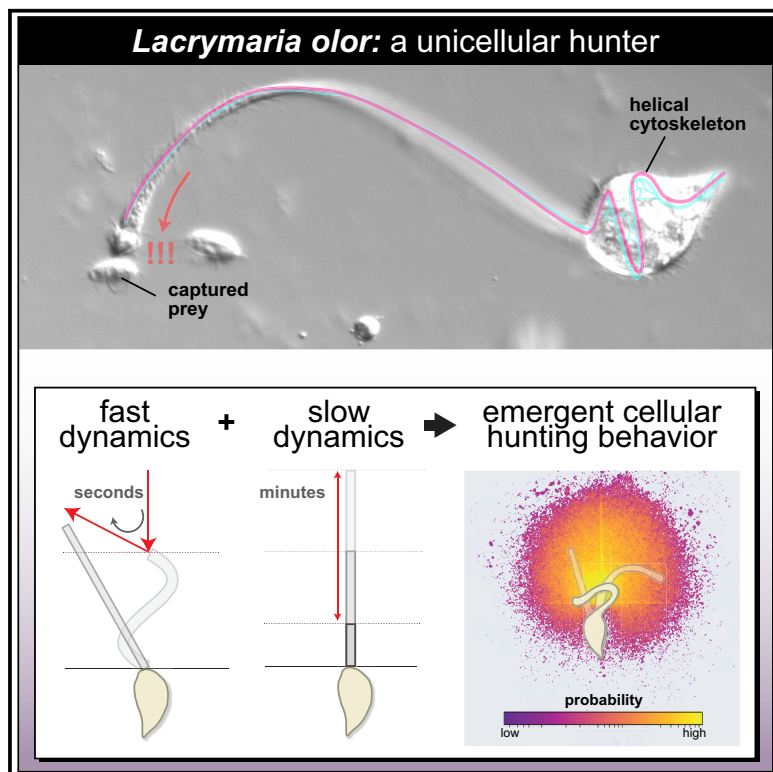


Coupled Active Systems Encode an Emergent Hunting Behavior in the Unicellular Predator *Lacrymaria olor*

Graphical Abstract



Authors

Scott M. Coyle, Elliott M. Flaum,
Hongquan Li, Deepak Krishnamurthy,
Manu Prakash

Correspondence

manup@stanford.edu

In Brief

Coyle et al. analyze how the swan-necked unicellular predator *Lacrymaria olor* uses extreme millisecond morphology dynamics to hunt for prey. The fast and slow mechanical responses of the cell's helical cytoskeleton to repeated cycles of compression and extension encode dense stochastic sampling of the local environment to locate and capture prey.

Highlights

- *Lacrymaria* is a unicellular predator that hunts using extreme morphology dynamics
- Computer vision digitizes millions of real-time sub-cellular postures during hunts
- Morphology dynamics result in dense stochastic sampling of the local environment
- Behavior emerges from fast and slow response of helical cytoskeleton to cyclic stress



Coupled Active Systems Encode an Emergent Hunting Behavior in the Unicellular Predator *Lacrymaria olor*

Scott M. Coyle,^{1,7} Elliott M. Flbaum,² Hongquan Li,³ Deepak Krishnamurthy,⁴ and Manu Prakash^{1,5,6,8,*}

¹Department of Bioengineering, Stanford University, Stanford, CA 94305, USA

²Graduate Program in Biophysics, Stanford University, Stanford, CA 94305, USA

³Graduate Program in Electrical Engineering, Stanford University, Stanford, CA 94305, USA

⁴Graduate Program in Mechanical Engineering, Stanford University, Stanford, CA 94305, USA

⁵Howard Hughes Medical Institute Faculty Scholar, Stanford University, Stanford, CA 94305, USA

⁶Chan Zuckerberg BioHub Investigator, Stanford University, Stanford, CA 94305, USA

⁷Present address: Department of Biochemistry, University of Wisconsin, 443 Babcock Drive, Madison, WI 53706-1544, USA

⁸Lead Contact

*Correspondence: manup@stanford.edu

<https://doi.org/10.1016/j.cub.2019.09.034>

SUMMARY

Many single-celled protists use rapid morphology changes to perform fast animal-like behaviors. To understand how such behaviors are encoded, we analyzed the hunting dynamics of the predatory ciliate *Lacrymaria olor*, which locates and captures prey using the tip of a slender “neck” that can rapidly extend more than seven times its body length (500 μm from its body) and retract in seconds. By tracking single cells in real-time over hours and analyzing millions of sub-cellular postures, we find that these fast extension-contraction cycles underlie an emergent hunting behavior that comprehensively samples a broad area within the cell’s reach. Although this behavior appears complex, we show that it arises naturally as alternating sub-cellular ciliary and contractile activities rearrange the cell’s underlying helical cytoskeleton to extend or retract the neck. At short timescales, a retracting neck behaves like an elastic filament under load, such that compression activates a series of buckling modes that reorient the head and scramble its extensile trajectory. At longer timescales, the fundamental length of this filament can change, altering the location in space where these transitions occur. Coupling these fast and slow dynamics together, we present a simple model for how *Lacrymaria* samples the range of geometries and orientations needed to ensure dense stochastic sampling of the immediate environment when hunting to locate and strike at prey. More generally, coupling active mechanical and chemical signaling systems across different timescales may provide a general strategy by which mechanically encoded emergent cell behaviors can be understood or engineered.

INTRODUCTION

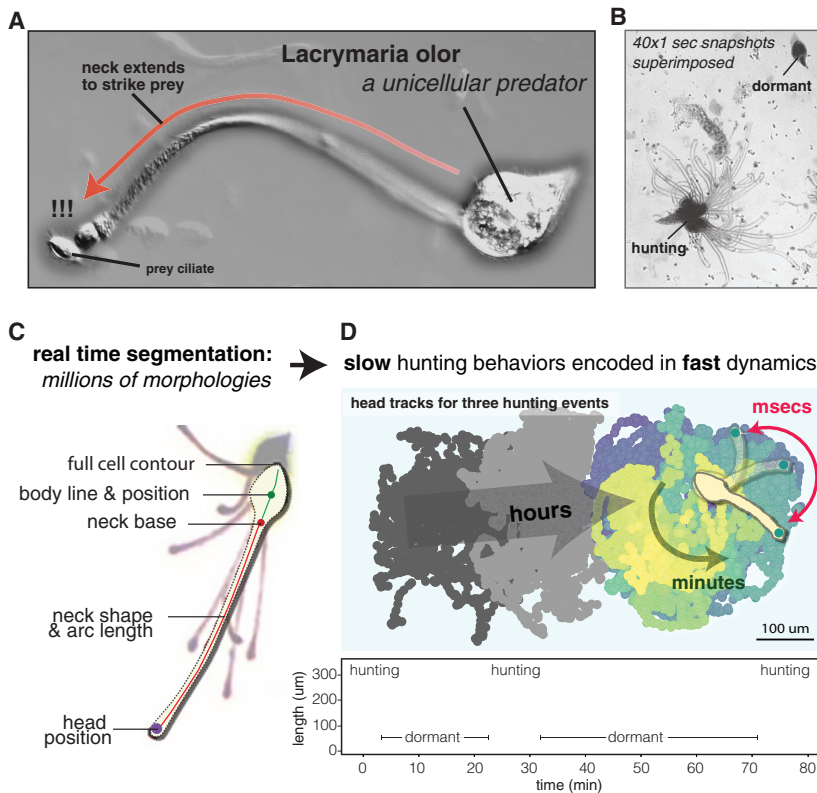
Cellular behavior emerges from the combined action of molecular systems that create structure, control mechanics, and respond to the environment [1–6]. While individual biochemical activities are often known, it is less clear how they are organized and coordinated to perform specific complex behaviors that develop over minutes, hours, or even days. Uncovering how cells couple active systems to build behavioral outputs would provide a fundamental link between the molecular and organismal functions of the cell and open up new frontiers for synthetic biology and molecular engineering.

Within Eukaryotes, unicellular ciliated protozoa perform complex, rapid animal-like behaviors, such as jumping, grabbing, and hunting [7–13]. Ciliates use two primary active systems to build their diversity of behaviors: motile cilia patterned on the cell surface and contractile protein networks that operate on the cell’s interior and cortex [14–19]. These are in turn organized in space through the geometry of the cell’s cortical cytoskeletal scaffolding [20, 21] and in time through signaling that rapidly regulates ciliary and contractile activities [8, 15, 18, 20, 21].

For ciliates whose behavior is largely defined by motility, such as *Paramecium*, analyzing swimming trajectories can provide insight into how behavior is encoded. For example, the “avoidance reaction” of *Paramecium* to bumping a wall is realized through electrical activity that regulates ciliary function [8, 15, 22–24]. However, other ciliates use morphology dynamics to build behavior, such as the ultrafast contractions of *Vorticella* and *Spirostomum* [25–28] or the manipulation of hunting proboscises for prey capture in *Dileptus* and *Lacrymaria* [29–32]. How morphologically defined ciliate behaviors are encoded is generally unknown.

Within predatory ciliates, *Lacrymaria olor* uses extreme cellular morphology dynamics to realize its hunting behavior. In the field, *Lacrymaria* attaches its cell body to debris and extends a small “head” and slender “neck” more than seven body lengths deep into the surrounding environment to locate





its prey [32]. As it hunts, the cell rapidly (sub-second) whips and retracts its neck as its head darts around to strike and subsequently engulf prey targets (Figure 1A; Video S1). Although the dynamic morphology of actively hunting *Lacrymaria* cells is complex, the subcellular architecture—a head, neck, and body—is simple enough to quantitatively analyze. The well-defined geometry, rich and fast morphological dynamics, and amenability to long-term imaging makes *Lacrymaria* ideal for exploring how higher-order morphological cell behaviors are encoded.

We established stable cultures of *Lacrymaria* and tracked the real-time morphology dynamics of individual cells in culture for hours, generating millions of morphology measurements that report on cellular behavior. This revealed that *Lacrymaria* hunts in periodic bursts of minutes-long activity we define as “hunting events,” in which the head densely samples nearly all locations within the radius of the cell neck while its body remains anchored. Rather than sequentially scan its environment, *Lacrymaria* uses a stochastic sampling strategy that is generated by repeated cycles of neck extension and contraction. We explore how this sampling arises from constraints on neck length and shape dynamics imposed by the cell’s underlying helical microtubule cytoskeleton. We suggest the neck acts like an elastic filament at short timescales but changes its fundamental length at longer timescales and present a model for how coupling these fast and slow components encodes the dense, efficient sampling that underlies *Lacrymaria*’s emergent hunting behavior.

Figure 1. The Unicellular Predator *Lacrymaria olor* Uses Ultrafast Morphology Dynamics to Hunt

(A) Stylized image of *Lacrymaria* cell in the act of striking prey.

(B) Image stack (40×1 s) of an actively hunting cell alongside a dormant cell.

(C) Digitization scheme for tracking *Lacrymaria* sub-cellular anatomy and shape.

(D) Visualization of the hunting behavior (head position and neck length) of a single cell over 90 min. Locations of the head are plotted in the lab reference frame and are color coded by time.

See also Figure S7, Video S1, and Video S2.

RESULTS

Lacrymaria Uses Fast-Timescale Morphology Dynamics to Perform Comprehensive Local Sampling over Longer Timescales as It Hunts for Prey

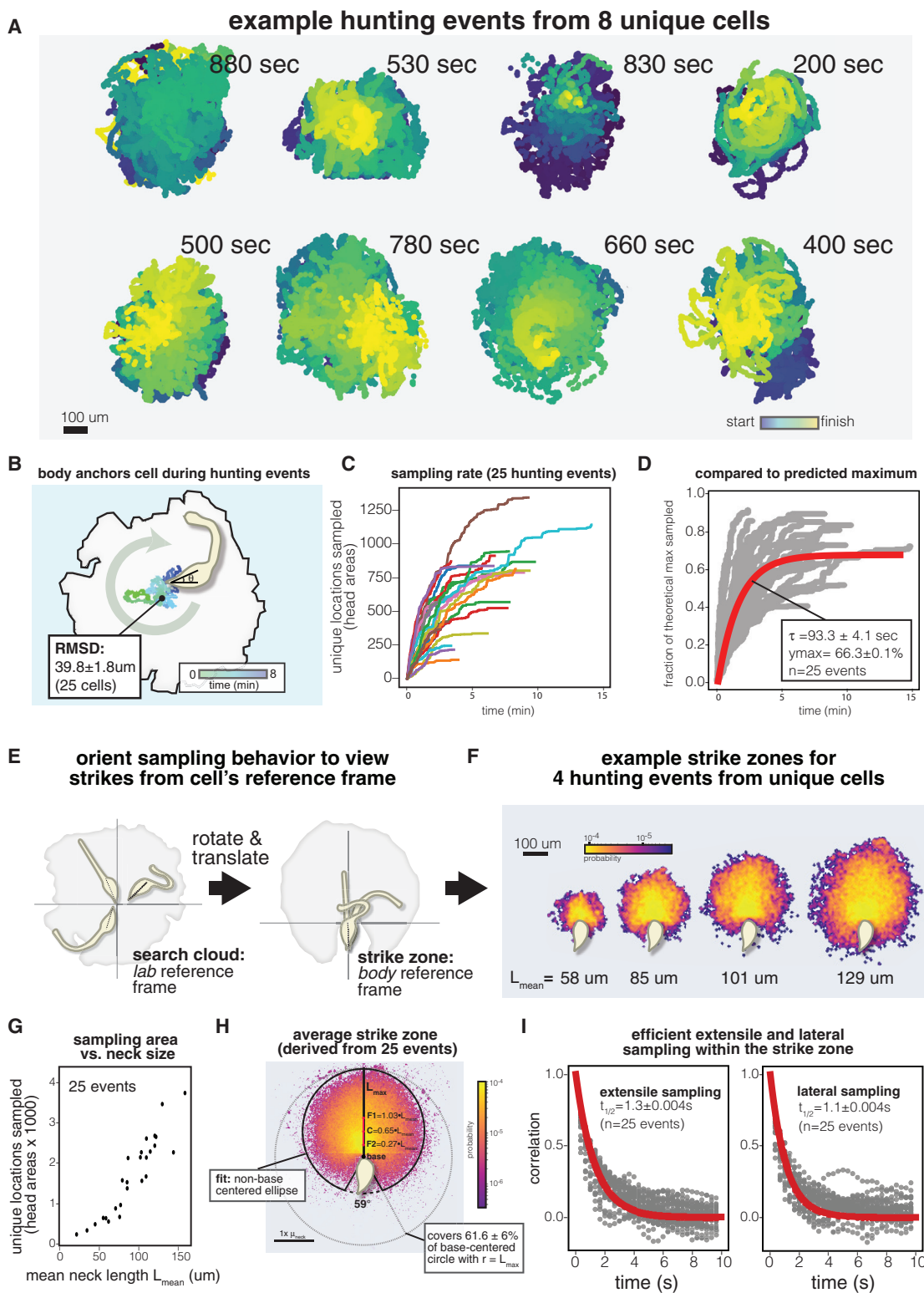
We grew small-scale microcultures of *Lacrymaria* in imaging plates for long-term observation. Cells perform native-like behaviors seen in the field [32, 33] and alternate between dormant states in which the cell neck is fully retracted and hunting states in which the head rapidly darts throughout the environment as the neck changes shape and length at hundreds of microns per second

(Figure 1B; Video S1). Superimposing snapshots of an actively hunting cell shows that the head and neck sample many locations in the environment, while the body remains mostly stationary (Figure 1B).

To study this quantitatively, we used computer vision [34, 35] to segment and track the sub-cellular posture—head, neck, and body—of individual cells in real-time over hours, generating millions of dynamic sub-cellular morphology measurements that report on cell behavior (Figure 1C; Video S2). We found that hunting occurred in periodic bursts of highly dynamic activity we define as “hunting events,” in which the cell’s neck length fluctuates rapidly for several minutes and the head densely samples the area within the radius of the cell neck (Figure 1D).

To understand how these “hunting events” are executed by the cell, we extracted 25 hunting events from 20 separate cells. This generated over 300,000 digitized sub-cellular postures spanning more than 170 min of real-time hunting activity. Despite variation in the detailed spatiotemporal structure of different hunting events, in every case sampling appears comprehensive—consistent and dense—in the area immediately within the radius of the cell’s neck (Figure 2A). Unique locations are initially sampled at a linear rate that saturates over time as cells begin to revisit locations (Figure 2C). By normalizing each sampling trace to a theoretical maximum based on neck size, we extracted an intrinsic timescale of 93.3 ± 4.1 s for saturation to $66.3\% \pm 0.1\%$ coverage of the theoretically accessible area (Figure 2D, $n = 25$ events).

During hunting events the cell body translates very little ($39.8 \pm 1.8 \mu\text{m}$, $n = 25$ events, Figure 2B) and is often in a fixed

**Figure 2. During a Hunting Event, *Lacrymaria* Comprehensively and Efficiently Samples Points from within an Expansive Strike Zone**

(A) Lab-reference frame sampling area plots derived from hunting events from 8 separate cells, color coded by time.

(B) Representative trace of the body displacement during a hunting event. See also Figure S1A.

(C) Dynamics for unique sampling for 25 hunting events.

(legend continued on next page)

orientation (Figure S1A). To explore sampling independent of body translation and rotation, we aligned head positions to a fixed body position and orientation to produce a “strike-zone” plot that reflects the points accessible from the cell’s own reference frame (Figure 2E). This revealed that cells can densely sample within a large region of space from a fixed position (Figure 2F; Figure S1C). The size of this strike zone increased with the average length of the neck, L_{mean} , indicating that *Lacrymaria* hunting behavior scales as cells grow (Figure 2G).

Using L_{mean} , we normalized and aligned 25 strike zones to define an average shape, range, and distribution (Figure 2H). We had anticipated that the average strike zone might correspond to a circle centered at the base of the neck with a radius corresponding to the cell’s maximum neck length. However, our ellipsoid fit was centered $0.65 \cdot L_{\text{mean}}$ from the base of the neck, spanning $61.6\% \pm 6\%$ ($n = 25$) of the coverage for a base-centered circle of radius L_{max} . This indicates the observed sampling must rely on points of flexibility along the neck about which it pivots or bends.

Importantly, points within the cell’s strike zone are rapidly and efficiently sampled, as the autocorrelation functions for the extensile and lateral components of the cell’s sampling decorrelated in seconds (Figure 2I; extensile: $\tau = 1.3 \pm 0.004$ s; lateral: $\tau = 1.1 \pm 0.004$ s; $n = 25$). Intuitively, this means that the head rapidly scrambles the location where it samples from during hunts.

Alternating Ciliary and Contractile Forces Drive the Motion of the Head and Deform the Neck on Slow and Fast Timescales

Because *Lacrymaria* is a microscopic single-celled organism, the hunting behavior we observe it perform is executed at low Reynolds number where viscous effects dominate over inertia [36]. To understand how the cell achieves dense stochastic sampling under these conditions, we examined the activities that control the motion of the head and neck during hunting events in more detail.

Lacrymaria’s “head” is covered with dense cilia that can generate strong hydrodynamic flows (Figure S1B; Video S3). Because the head is tethered to the end of the neck, it is not free and instead acts like a swimmer on a string. Indeed, when we aligned our swim velocity data for the head to the orientation of the neck, the distribution was asymmetric and biased toward motion oriented in line with the neck (forward/reverse) compared to normal to it (left/right) (Figure 3A; 1.92 ± 0.11 -fold bias, $n = 25$ events). Using high-speed differential interference contrast (DIC) imaging, we found that the head and neck take turns applying forces that drive these motions (Figure 3C). In *extension* mode, the head cilia are active and apply a pulling force to the end of the neck. In *retraction* mode, the head cilia become

inactive, the neck cilia reverse orientation, and a strong contraction pulls the head and neck back toward the body (Figure 3B; Video S3). The associated head-speed distributions were mean centered, with a range of mean head speeds observed across different events (Figure 3D), and similar trends were observed for the neck-length distributions (Figure 3E). A positive correlation between mean neck length and head speed was observed (Figure 3F).

Because the neck-length distributions were broad, we carefully examined their associated dynamics. At short timescales, rapid cycles of extension and retraction appear to be centered about a local mean length (Figure 3G). However, at longer timescales the length about which these cycles occur appears to change (Figure 3G; Figure S2A). This suggests a natural decomposition into a slow-varying “local mean length” (L_0) component and a fast-varying “displacement” ($\Delta L_0 = L_{\text{obs}} - L_0$) component, analogous to the AC and DC components of a dynamic electrical signal. By detrending with a sliding window of 15 s, L_0 explained $28.6\% \pm 0.3\%$ of the variance in the observed length distribution, while ΔL_0 explained $67.8\% \pm 0.3\%$ of the variance ($n = 25$ events) (Figures 3H–3K; Figure S2B).

To understand the origin of these fast and slow components, we examined the cytoskeletal architecture that supports the morphological changes of the cell. The cortical microtubules of *Lacrymaria* have been reported to be arranged in a stable helical structure [33, 37, 38]. We visualized a more complete cytoskeleton by immunostaining for both tubulin and centrin-type (myoneme) cytoskeletal proteins in extended and retracted cells (Figure 4A; Figure S3; Video S4). The microtubule scaffolding of the cell adopts a continuous helical geometry that runs from the base of the cell to the tip of the neck, transitioning sharply from small helical pitch in the body to large helical pitch in the neck. We also discovered a network of undulating centrin-rich fibers juxtaposed with the microtubule network (Figure 4C). These fibers closely follow the helical geometry of the microtubule network in the neck but transition to mesh-like cross-links in the body (Figure 4B). Centrin-rich filament networks are typical components of ultrafast calcium-responsive contractile structures in ciliates such as the spasmonemes of *Vorticella* and the myonemes of *Stentor* [16–19, 39].

Since the cytoskeleton is continuous, the cell body and neck actually correspond to different geometries of the same underlying cytoskeletal network (Figure 4D). The helical geometry we observe allows for two modes by which the apparent length L_{obs} of the neck can change (Figure 4E). In mode 1, segments of cytoskeleton could interconvert between body-like (small pitch, large radius) and neck-like geometries (large pitch, small radius), changing the total amount of cytoskeleton with neck-like geometry (denoted $S_0 > S'_0$), and consequently L_{obs} . In

(D) The data from (C), normalized to a theoretical maximum number of points that could be sampled based on the maximum neck length and the positions of the body during the event.

(E) Scheme for aligning the cell’s sampling behavior to the reference frame of the cell body to produce a “strike zone” of the points the cell can strike from a fixed position.

(F) Strike-zone plots for 4 cells of different indicated sizes. See also Figure S1C.

(G) Correlation between size of the cell’s sampling area mean neck length.

(H) Average strike-zone plot obtained by normalizing all strike-zone plots to their mean neck length. The dotted line shows the range expected for a circle of radius L_{max} centered at the base of the cell neck. The solid line shows the ellipse of best fit to the boundary of the empirically derived average sampling area.

(I) Autocorrelation plots for extensile and lateral components of sampling, derived from 25 cells (gray dots) and globally fit to an exponential (red line).

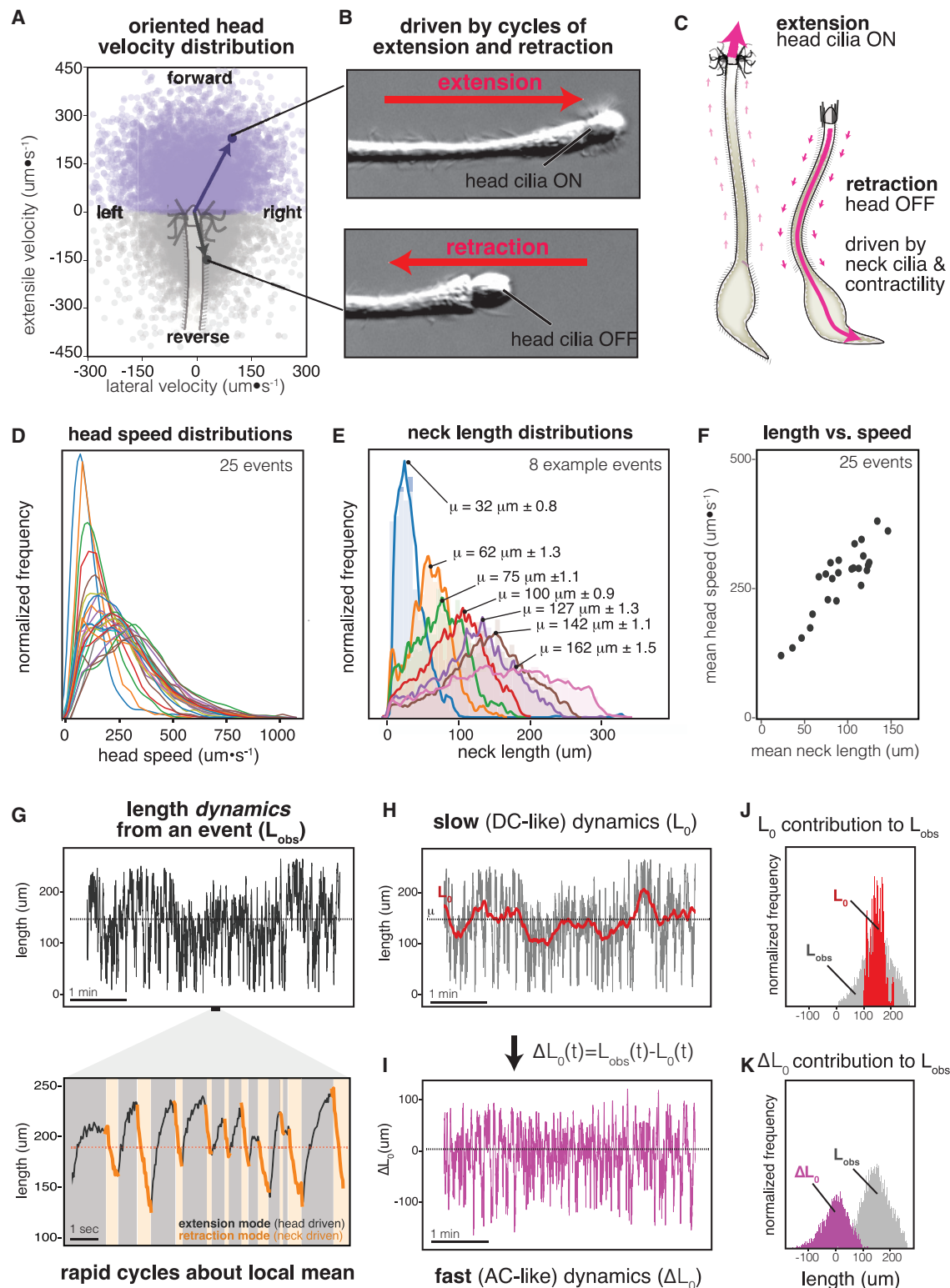


Figure 3. The Head and Neck Take Turns Applying Ciliary and Contractile Forces that Drive the Motion of the Head and Deform the Structure of the Neck

(A) Head velocity distribution of a representative cell oriented to the tip of the cell neck. Forward velocities are purple; reverse velocities are gray.

(B) DIC images of the cell head and neck while moving in the forward or reverse direction.

(C) Diagram illustrating how the head and neck take turns driving the extension and retraction of the head.

(legend continued on next page)

mode 2, the cytoskeleton already in a neck-like geometry (S_0) could be further deformed to increase or decrease its aspect ratio. In this case, there is no change in S_0 but the cell's apparent neck length L_{obs} can change.

Because mode 1 is associated with a large, local rearrangement of the cytoskeletal geometry and may also require disruption of the centrin mesh, it is expected to be more energetically expensive than mode 2. As such, we hypothesize that the slow (L_0) and fast (ΔL_0) components of *Lacrymaria*'s length dynamics reflect mode 1 and mode 2 rearrangements of the cytoskeleton, respectively. In support of this, note that, because a dormant cell's entire cytoskeleton is in the body-like geometry, initiating or terminating a hunting event would be expected to be dominated by mode 1 rearrangements. Consistently, hunting events begin with a slow and steady increase in L_0 (Figure 4F, mode 1 extension: $0.78 \pm 0.03 \mu\text{m} \cdot \text{s}^{-1}$, $n = 10$) and terminate with a slow and steady decrease in L_0 (Figure 4G, mode 1 retraction: $0.4 \pm 0.04 \mu\text{m} \cdot \text{s}^{-1}$, $n = 10$). These rates are consistent with how L_0 varies in amplitude during the peak stage of a hunting event.

Mode 2 rearrangements are expected to be geometrically constrained by the amount of cytoskeleton currently available in the neck-like configuration (S_0) (Figure 4E). In between the initiation and termination stages, the spread in L_0 distribution becomes tight (Figure 4H, $\mu_{\text{QR}} = 33 \pm 3.8 \mu\text{m}$, $n = 25$ events) as large and rapid cycles of extension and retraction about the local value of L_0 dominate the observed length dynamics. If these fast dynamics correspond to mode 2 rearrangements, then larger values of L_0 should be associated with a larger range of displacement ΔL_0 . As predicted, L_0 is linearly correlated with the mean displacement (Figure 4I; $r^2 = 0.91$ for extension; $r^2 = 0.95$ for retraction), suggesting ΔL_0 dynamics are likely mode 2 type changes in cytoskeleton aspect ratio. This is also consistent with changes in neck width observed during rapid extension and retraction cycles (Figure S3E).

At Short Timescales, *Lacrymaria*'s Neck Acts Like an Elastic Filament under Load, Adopting Shapes that Facilitate Reorientation

Based on our analysis, for short timescales we propose an explicit physical analogy between the neck and a slender elastic filament of length L_0 (Figure 5A). The physics of such filaments predicts that, under compression ($L_{\text{obs}} < L_0$), there should be an associated harmonic series of buckling modes in which (1) higher-order modes require greater forces to be triggered, and (2) the force requirements to activate modes should decrease with increasing L_0 [40].

To test, we performed principal-component analysis (PCA) on our neck shape data to identify the natural eigenshapes modes

of the neck independent of length (Figure 5B; Figure S4) [41]. The first four eigenshape modes explain >98% of the shape variance, 90% by the first two modes (Figure 5B; Figure S4C). The PCA-derived shapes form a series of harmonic modes that could be fit to the buckling modes of an Euler-Bernoulli beam (first mode: $r^2 = 0.993$; second: $r^2 = 0.986$; third: $r^2 = 0.861$; fourth: $r^2 = 0.771$; Figure S4B) and were easily recognizable in hunting cells (e.g., Video S5).

Expectedly, these shape modes were most prevalent when the neck was in a compressed state ($L_{\text{obs}} < L_0$), as plotting shape mode activation as a function of displacement from L_0 revealed a sharp transition near $\Delta L_0 = 0$ ($I_{1/2} = -5.7 \pm 0.1 \mu\text{m}$, $k = 0.10 \pm 0.001 \mu\text{m}^{-1}$ for shape mode 1; $I_{1/2} = -4.6 \pm 0.1 \mu\text{m}$, $k = 0.12 \pm 0.001 \mu\text{m}^{-1}$ for shape mode 2; $n = 25$) (Figure 5C). As predicted, the average amplitude of the modes decreased monotonically with mode number (Figure 5D). Furthermore, as L_0 increased, the average amplitude of the higher-order modes increased, consistent with the expected length-dependent behavior of slender elastic filaments (Figure 5D).

The extensile behavior of the neck is more complex to analyze because it reflects the contributions of stretching, bending, and twisting forces acting on a complex viscoelastic material. Nevertheless, the physical analogy predicts that, if the head applies a constant extensile force, its speed will slow down for $L_{\text{obs}} > L_0$ [40]. We extracted 101 well-resolved instances of this type of extension from our data and found that, as expected, L_{obs} approached its final extended state with exponential dynamics ($t = 0.55 s \pm 0.03 s$, $n = 101$) coincident with the head speed decaying at a similar timescale ($t = 1.12 \pm 0.03 s$, $n = 101$) (Figure 5E).

These statistical analyses agree with how ΔL_0 dynamics and shape mode dynamics are correlated. In the dynamics, shape mode amplitudes dramatically increase whenever $L_{\text{obs}}(t) < L_0(t)$ and dramatically decrease whenever $L_{\text{obs}}(t) > L_0(t)$ (Figure 5F). These cycles of compression and shape mode activation have ramifications for sampling behavior. When shape mode amplitudes are 0, the neck is straight. However, for non-zero amplitudes, the tip of the neck points away from the end-to-end axis, reorienting the head's extensile trajectory (Figure 6A). The empirical shape distribution from our data corresponds to a wide range of head orientations (Figure 6B). This breadth arises from the fact that reorientation is proportional to the amplitude of each shape mode (Figure 6C) and that mode activation is transient (<0.20 s) as judged by autocorrelation (Figure 6D). As such, we find specific regions within the cell's strike zone are strongly correlated with contributions from shape modes (Figure 6E).

Together, different patterns and sequences of shape mode usage facilitate "sub-behaviors" that drive sampling of the cell's

(D) Head-speed distributions from 25 separate hunting events.

(E) Neck-length distributions from 8 separate hunting events.

(F) Correlation between neck length and head speed.

(G) Length dynamics from a 5-min window of a representative hunting event, with a zoom in showing a 10 s window.

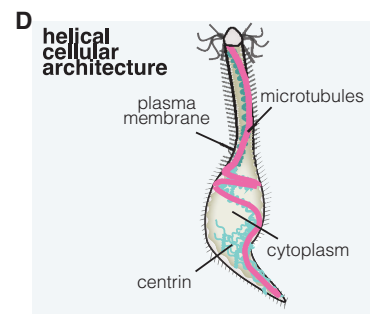
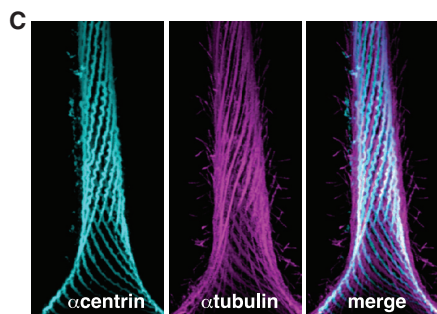
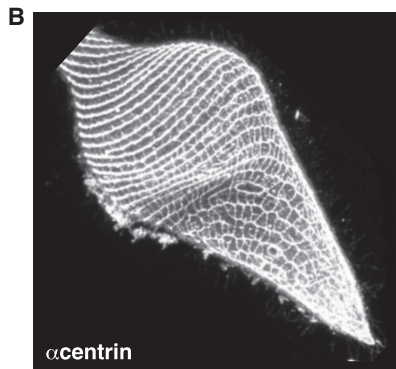
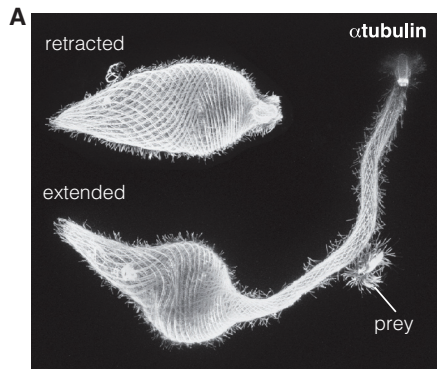
(H) The moving average (15 s window) for the neck length (L_0) from (G) in red superimposed on the overall dynamics in gray.

(I) The fast dynamics (ΔL_0) that remain after subtracting off the slow-moving average.

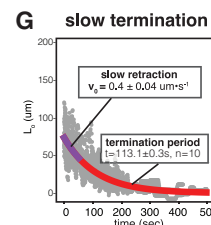
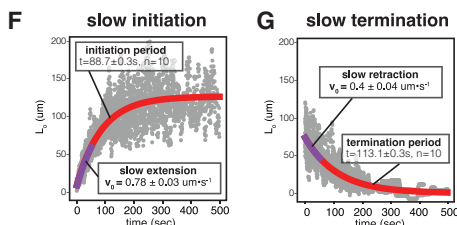
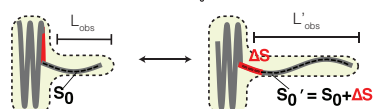
(J) Length distribution for the entire hunting event (gray) and the contribution of L_0 to the variation (red).

(K) As in (J) but with the contribution of ΔL_0 to the observed length distribution in purple.

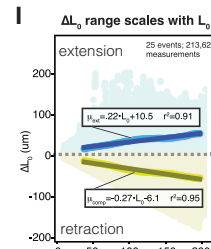
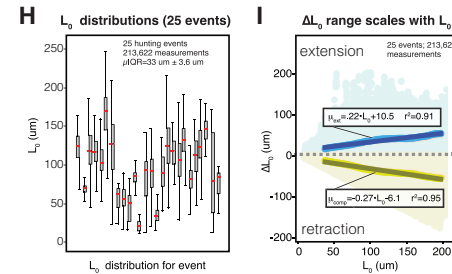
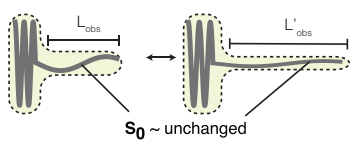
See also Figure S2 and Video S3.



E ① **SLOW I** unspool from body:
changes total amount of
cytoskeleton in the cell's neck
→ changes L_0



② **FAST I** change neck aspect ratio:
rearranges cytoskeleton that
is already in the cell neck
→ does not change L_0



immediate surroundings (Figure 6F). These include low-amplitude buckling that results in minor, localized reorientation, high-amplitude buckling that produces whipping that significantly scrambles the next trajectory of the head, or sustained activation of the first shape mode to provide a steering activity that can pivot the cell left or rightward.

Coupling Contractile and Ciliary Activities across Fast and Slow Timescales Underlies *Lacrymaria*'s Emergent Sampling Behavior

The fact that *Lacrymaria*'s neck acts like an elastic filament at short timescales but can change its fundamental length L_0 over longer timescales suggests a simple mechanical mechanism to realize its dense, near-random sampling. Fast cycles of

Figure 4. *Lacrymaria*'s Neck and Body Are Supported by Distinct Geometries of a Continuous Helical Cytoskeleton, Which Can Undergo Two Modes of Rearrangement

(A) Maximum z-projection of two *Lacrymaria* cells (digitally juxtaposed) immunostained for acetylated tubulin.

(B) Maximum z-projection of an extended *Lacrymaria* cell immunostained for centrin.

(C) Maximum z-projection of an extended *Lacrymaria* neck immunostained for acetylated tubulin (cyan) and centrin (magenta).

(D) Schematic of the helical cellular architecture of *Lacrymaria* that supports the morphological rearrangements that occur during hunting events.

(E) Schematic depicting two distinct modes by which the cytoskeleton can rearrange to change the observed length of *Lacrymaria*'s neck. A slow mechanism that converts a segment of cytoskeleton in the body configuration into one in the neck configuration and a fast mechanism that rearranges the existing pool of cytoskeleton already in the neck configuration.

(F) The initial rates of length change measured during the early slow initiation period of a hunting event ($n = 10$ events).

(G) The initial rates of length change measured during the early slow termination period of a hunting event ($n = 10$ events).

(H) Box and whisker plots for the distribution of L_0 for 25 hunting events.

(I) Distribution (points) and mean (line) extensile or contractile displacement about L_0 (ΔL_0) as a function of the magnitude of L_0 .

See also Figure S3 and Video S4.

compression, buckling-induced reorientation, and extension rapidly sample a range of trajectories about L_0 , while slow changes in L_0 move the location in space about which this sampling occurs (Figure 7A). To explore whether this coupling could recapitulate the cell's sampling area, we used simple geometry and our empirical length and shape distributions to simulate the trajectories available to the head as it sweeps through a range of L_0 values. Although we neglect the complexity of extension and correlations between trajectories, we nonetheless recover a strike zone with similar shape and coverage area to empirical observation (Figure 7B; Figure 2H). Importantly, if shape probabilities are set to 0, the simulated cell only samples back and forth along a line in front of itself, while, if L_0 is fixed in one value, it searches a more localized region of space (Figure S6).

To experimentally test the importance of this coupling, we took advantage of the fact that most ciliates use calcium ions to control ciliary activity and contractility [15, 18, 42, 43] and confirmed that this applied to *Lacrymaria* (Figure S5; Video S6). We then screened calcium channel inhibitors and found that low concentrations of cobalt chloride (1 mM) specifically

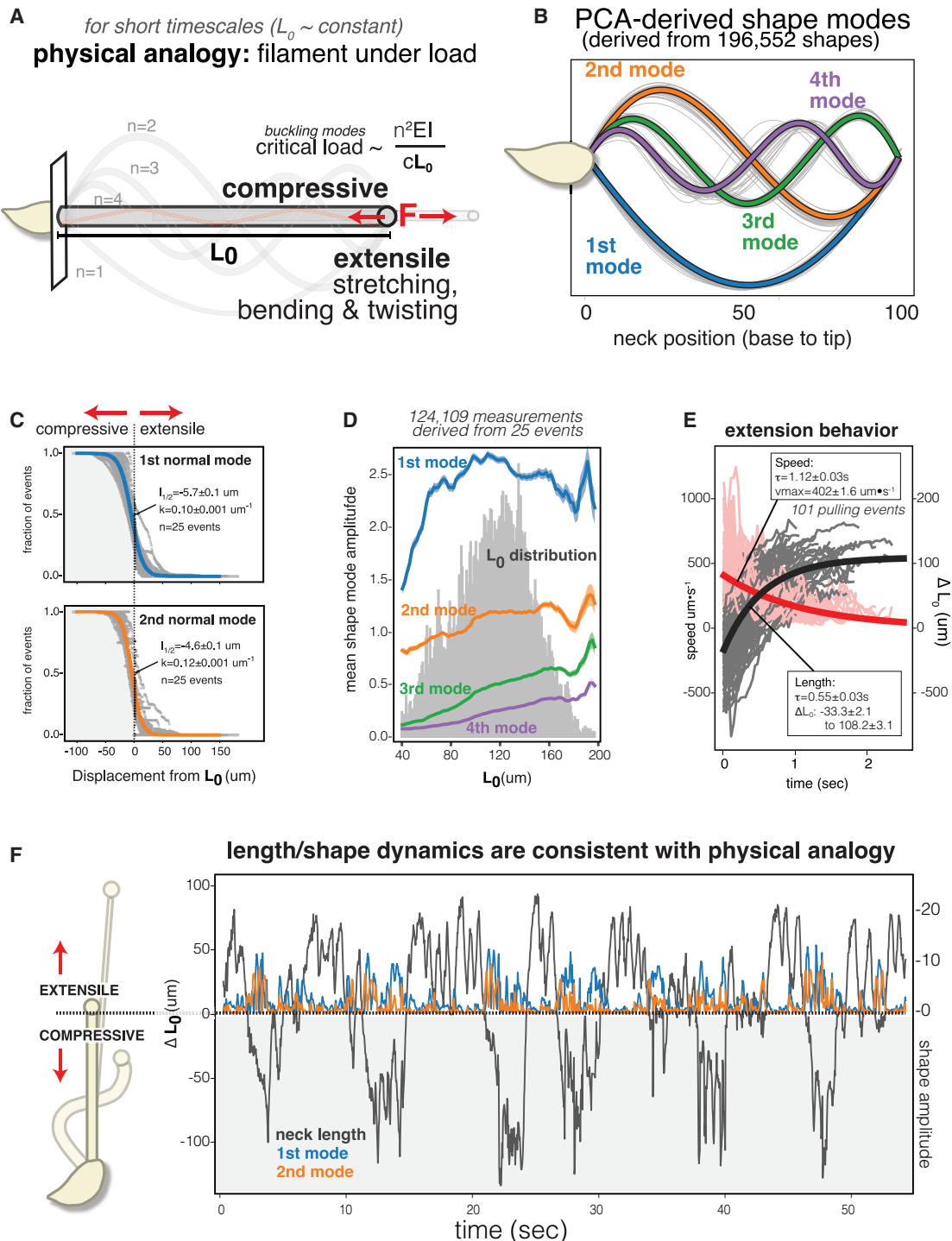


Figure 5. At Short Timescales, *Lacrymaria*'s Neck Behaves Like an Elastic Filament under Compressive or Extensile Loading

- (A) Physical analogy between *Lacrymaria*'s neck and an elastic filament of length L_0 under load.
- (B) The first four eigenshape normal modes in the harmonic series obtained from PCA analysis (globally fit shapes shown in color; shapes from individual cells in gray).
- (C) Fraction of strong shape mode occurrence (>2.5 amplitude) as a function of displacement from L_0 for 25 hunting events (gray), with sigmoid fits and associated parameters shown (color) for the first and second shape modes.
- (D) Average amplitude of the first four shape modes as a function of L_0 . The distribution of accessible L_0 values is shown as a gray histogram.
- (E) Extension behavior of the head speed (pink) and neck length (gray) derived from 101 pulls that we extracted from the data. Fits to an exponential for head speed (red) and neck length (black) are shown.
- (F) Length (displacement from L_0) and shape dynamics (blue: first mode; orange: second mode) during 1 min of hunting activity.
 See also Figure S4 and Video S5.

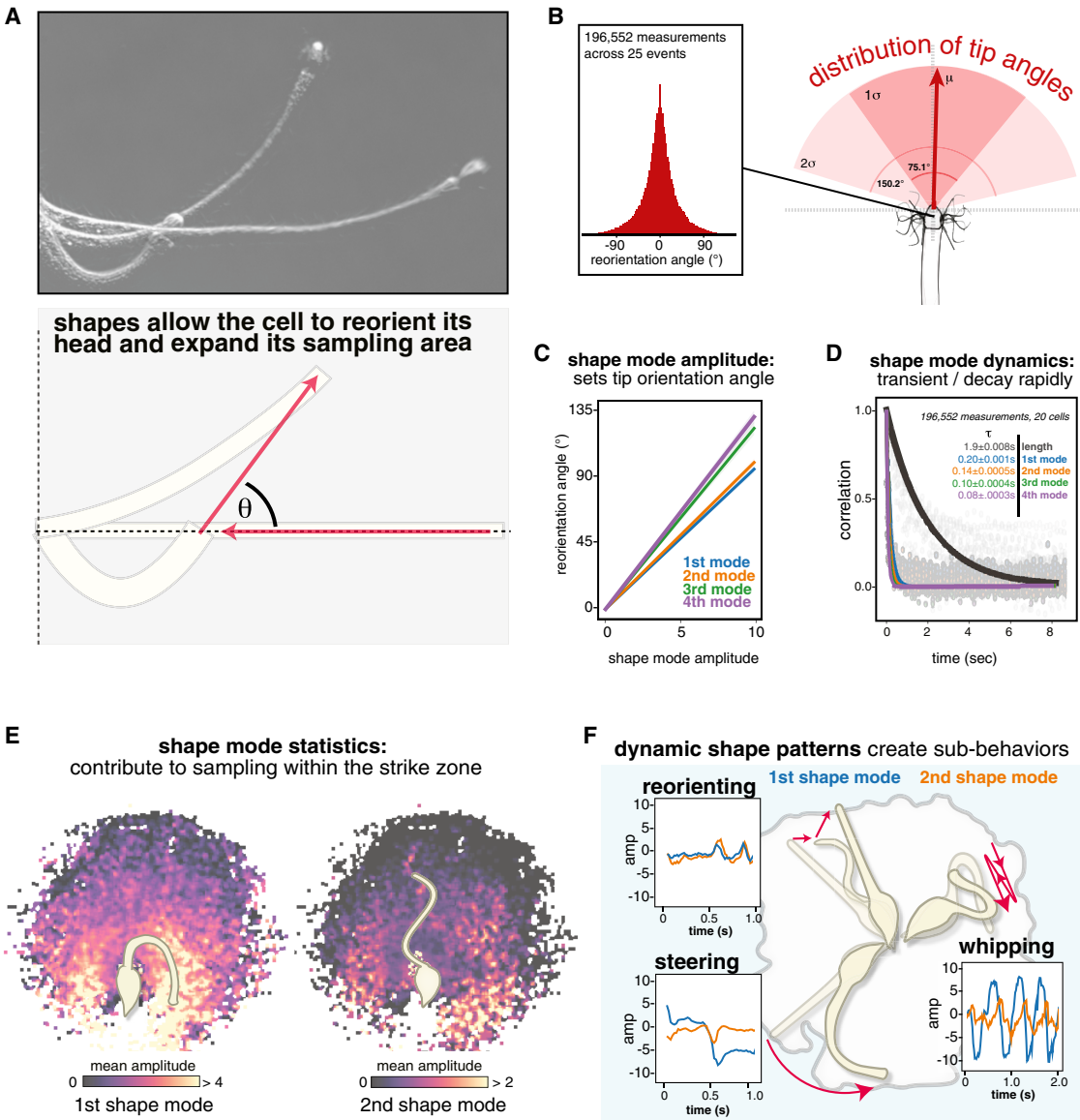


Figure 6. Compression of the Neck Scrambles the Direction of the Head's Extensile Trajectory, Expanding Its Sampling Area

- (A) 3 superimposed DIC images of a cell during a cycle of retraction, compression, and extension and a schematic depicting the changes in trajectory.
- (B) Distribution of reorientation angles arising from neck shape obtained by pooling data from 25 hunting events. The associated range of tip angles is also depicted.
- (C) A plot of the tip reorientation angle as a function of amplitude for the first four eigenshapes.
- (D) Autocorrelation functions for length (gray) or amplitudes of each eigenshape mode (colors) during search (points) and associated exponential fit (line).
- (E) Strike zones for a representative hunting event recolored by the average amplitude of the first or second eigenshape mode of the neck when sampling that point.
- (F) Experimentally observed patterns of shape mode usage that facilitate sub-behaviors such as reorientation, whipping, or steering.

arrested *Lacrymaria*'s fast dynamics (Figure 7C; Video S7) [44]. Cobalt-treated cells continued to perform periodic hunting events for hours (Figure 7D; Video S7) but lacked rapid length and shape dynamics (Figure 7E). DIC microscopy indicated that treated cells could still regulate their ciliary activity but could not rapidly contract their necks to transiently activate shape modes (Video S7). To measure the consequences of this on sampling, we digitized the head positions from 10 cells pre-

and post-cobalt treatment and observed highly biased, correlated sampling post-treatment (Figure 7F). The sampling autocorrelation functions showed an 11-fold increase in the scrambling time for the extensile component (Figure 7G; pre- τ : 0.52 ± 0.04 s; post- τ : 5.8 ± 0.5 s; $n = 10$) and a 7-fold increase for the lateral component (Figure 7H; pre- τ : 0.84 ± 0.02 s; post- τ : 6.6 ± 0.7 s; $n = 10$). Together, these data support our model that coupling active systems across fast and slow

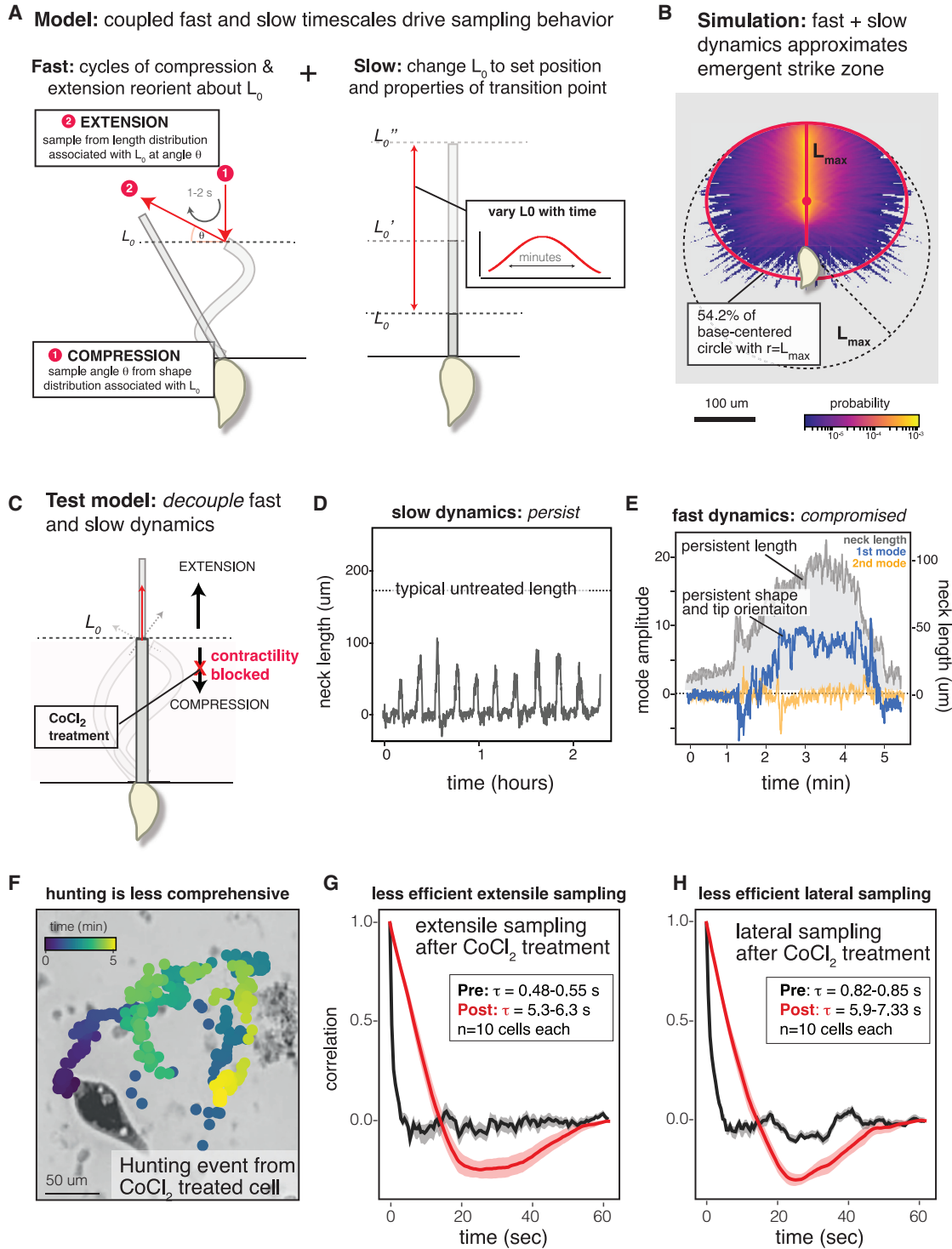


Figure 7. Coupling Active Systems across Fast and Slow Timescales Encodes *Lacrymaria*'s Emergent Sampling Behavior

- (A) Proposed model: fast cycles of compression and extension trigger buckling and sample trajectories about L_0 ; slower variations in L_0 change the location in space about which trajectories are sampled.
- (B) Sampling area from a simple simulation of (A) based on geometry and the empirical length and shape distributions. The simulated sampling area was fit to an ellipse (red).
- (C) Schematic showing that cobalt chloride treatment disrupts *Lacrymaria*'s rapid cycling.
- (D) Representative length dynamics for a single cell over the course of 2 h.
- (E) Representative length and shape dynamics for a single hunting event from (D).

(legend continued on next page)

timescales is important for producing *Lacrymaria*'s emergent sampling behavior.

DISCUSSION

By analyzing the real-time morphology dynamics of the unicellular predator *Lacrymaria* over hours, we found that rapid motions of the cell's head and neck are integrated over several minutes to perform a “hunting event,” an emergent cellular behavior that comprehensively and efficiently samples from within the radius of the cell's neck. These events are driven by patterns of ciliary and contractile forces that appear to rearrange the cell's helical cytoskeleton on fast and slow timescales. We hypothesize that at short timescales the neck behaves analogous to an elastic filament under load, such that compressive forces trigger buckling that reorients the head's angle for its subsequent extension. At longer timescales, the fundamental length of this filament can change, altering the point in space where the transition to compression occurs. We propose that coupling fast and slow dynamics together allows the cell to sample the breadth of orientations and trajectories that establish its dense stochastic sampling behavior.

The data-driven phenomenological model we present for *Lacrymaria*'s sampling behavior suggests specific biochemical and biophysical questions for future experimental and theoretical inquiry. Are the slow length dynamics we observe an emergent consequence of differences in the pattern of extensile versus contractile forces integrated over time, or do other active systems, such as motor proteins, contribute? How does the cell's molecular architecture set an appropriate neck stiffness to allow buckling modes to effectively reorient the head? How is the critical helical cytoskeletal geometry established by the cell? Can hunting behavior be tuned by regulating the pattern of forces that manipulate its structure? Our present analysis provides a starting point with which to approach these exciting questions.

How do we interpret *Lacrymaria*'s sampling behavior in the broader context of hunting and foraging strategies [45–49]? *Lacrymaria* is known to capture preys that include fast motile swimmers as well as stationary ciliates and small amoebas that sit and feed on the decaying matter [32, 33, 37]. By attaching itself to detritus and rapidly striking at diverse locations within its surroundings, *Lacrymaria* is poised to intercept swimming and stationary preys (Video S1) that might be drawn to the nutritional oases in which *Lacrymaria* resides. Additionally, the uniform and near-random sampling of the environment we report was observed in prey-free conditions. In the presence of environmental cues, it is possible that *Lacrymaria* might bias its sampling to increase the probability of prey capture. Our analysis of *Lacrymaria*'s ground state behavior provides the framework to understand how the timing of compression, reorientation, and extension might be regulated to bias

behavior, akin to a tethered version of “run and tumble” models of *E. coli* motility or sperm navigation [50, 51].

In field recordings, *Lacrymaria*'s neck can bend around obstructions and poke through debris as it hunts (Video S1), a phenomenon that can be understood from our present analysis and model. If the neck becomes pinned or restrained, a new barrier to cytoskeletal rearrangement is introduced analogous to the body/neck junction, such that the free portion of the neck will behave locally like an elastic filament. If the cell frees itself, the barrier to rearrangement is removed and the neck's original behavior is restored. Thus, in addition to the natural degrees of freedom intrinsic to the cell's geometry, *Lacrymaria* can likely make use of the environment itself to further constrain its sampling.

The importance of mechanics in organizing cellular behavior in *Lacrymaria* we describe is in contrast to other mechanisms that rely on centralized information processing and transcription. For microscale molecular machines like *Lacrymaria* and other ciliates, the ultrafast timescales of operation and scaling requirements may leave little choice but to employ mechanical strategies to encode key aspects of behavioral output. In mammalian cells, such mechanically encoded strategies likely cooperate with transcriptionally driven processes to organize longer timescale cellular behavior [6, 52]. As such, we anticipate efforts to engineer complex behaviors into molecular and cellular machines may benefit from incorporating similar mechanical strategies into designs.

STAR★METHODS

Detailed methods are provided in the online version of this paper and include the following:

- KEY RESOURCES TABLE
- LEAD CONTACT AND MATERIALS AVAILABILITY
- EXPERIMENTAL MODEL AND SUBJECT DETAILS
 - Cell lines
- METHOD DETAILS
 - Detailed culture methods
 - Immunostaining and Confocal imaging
 - High-speed imaging
 - Flow-trace imaging of tracer particles
 - Darkfield timelapse imaging
 - Image processing, segmentation, tracking, and data processing and modeling
 - Perturbation experiments
- QUANTIFICATION AND STATISTICAL ANALYSIS
- DATA AND CODE AVAILABILITY

SUPPLEMENTAL INFORMATION

Supplemental Information can be found online at <https://doi.org/10.1016/j.cub.2019.09.034>.

(F) Representative point sampling behavior for a cobalt treated cell, showing the points visited over 5 min color coded by time.

(G) Autocorrelation functions for extensile sampling pre- (black) and post- (red) cobalt treatment and associated integral timescale ($n = 10$).

(H) As in (G) but for lateral sampling.

See also Figure S5, Figure S6, Video S6, and Video S7.

ACKNOWLEDGMENTS

S.M.C. is a Helen Hay Whitney Fellow supported by the Helen Hay Whitney Foundation. E.M.F. is supported by a Stanford Biophysics NIH training grant, H.L. by a Stanford Bio-X SIGF fellowship, and D.K. by a Stanford Bio-X Bowes Fellowship. This work was supported by NSF CCC grant (DBI- 1548297) to M.P., US Army Research Office grant (W911NF-15-1-0358) to M.P., CZI BioHub Investigator Program to M.P., Keck Foundation Research Grant to M.P., and the Howard Hughes Medical Institute to M.P. We especially thank R. Yanase for providing starter cultures and invaluable protocols and R. Howie for general culturing advice. We thank Reviewer #1 for suggesting analyses that significantly improved this work. We thank members of the Prakash Lab, A. Weeks, L. Pack, B. Benson, and L. Ui for helpful discussions and comments.

AUTHOR CONTRIBUTIONS

Conception and Design, S.M.C. and M.P. with input from all co-authors; Live Imaging, S.M.C. with assistance from H.L.; Segmentation, Tracking, and Analysis, S.M.C. with assistance from D.K. and H.L.; Immunofluorescence Studies, E.M.F. with assistance from S.M.C.; Conception and Design of Models, S.M.C., E.M.F., D.K., and M.P.; Writing – Manuscript, S.C., E.M.F., and M.P. with input from all co-authors.

DECLARATION OF INTERESTS

The authors declare no competing interests.

Received: March 6, 2019

Revised: July 11, 2019

Accepted: September 13, 2019

Published: October 31, 2019

REFERENCES

- Lim, W.A., Lee, C.M., and Tang, C. (2013). Design principles of regulatory networks: searching for the molecular algorithms of the cell. *Mol. Cell* **49**, 202–212.
- Tyson, J.J., Chen, K.C., and Novak, B. (2003). Sniffers, buzzers, toggles and blinkers: dynamics of regulatory and signaling pathways in the cell. *Curr. Opin. Cell Biol.* **15**, 221–231.
- Herrmann, H., Bär, H., Kreplak, L., Streikov, S.V., and Aebi, U. (2007). Intermediate filaments: from cell architecture to nanomechanics. *Nat. Rev. Mol. Cell Biol.* **8**, 562–573.
- Shelley, M.J. (2016). The dynamics of microtubule/motor-protein assemblies in biology and physics. *Annu. Rev. Fluid Mech.* **48**, 487–506.
- Murrell, M., Oakes, P.W., Lenz, M., and Gardel, M.L. (2015). Forcing cells into shape: the mechanics of actomyosin contractility. *Nat. Rev. Mol. Cell Biol.* **16**, 486–498.
- Keren, K., Pincus, Z., Allen, G.M., Barnhart, E.L., Marriott, G., Mogilner, A., and Theriot, J.A. (2008). Mechanism of shape determination in motile cells. *Nature* **453**, 475–480.
- Slabodnick, M.M., and Marshall, W.F. (2014). Stentor coeruleus. *Curr. Biol.* **24**, R783–R784.
- Kung, C., Chang, S.Y., Satow, Y., Houten, J.V., and Hansma, H. (1975). Genetic dissection of behavior in paramecium. *Science* **188**, 898–904.
- Hara, R., and Asai, H. (1980). Electrophysiological responses of Didinium nasutum to Paramecium capture and mechanical stimulation. *Nature* **283**, 869–870.
- Dijk, T.V., Modeo, L., and Verni, F. (2008). *Microbial Ecology Research Trends* (Nova Biomedical Books).
- Gilbert, J.J. (1994). Jumping behavior in the oligotrich ciliates *Strobilidium velox* and *Halteria grandinella*, and its significance as a defense against rotifer predators. *Microb. Ecol.* **27**, 189–200.
- Grell, K.G. (1973). *Protozoology* (Springer-Verlag).
- Jennings, H.S. (1906). *Behavior of the Lower Organisms* (Columbia University Press).
- Machemer, H., and Sugino, K. (1989). Electrophysiological control of ciliary beating: A basis of motile behaviour in ciliated protozoa. *Comp. Biochem. Physiol. Part A. Physiol.* **94**, 365–374.
- Naito, Y., and Kaneko, H. (1973). Control of ciliary activities by adenosine-triphosphate and divalent cations in triton-extracted models of *Paramecium caudatum*. *J. Exp. Biol.* **58**, 657–676.
- Mahadevan, L., and Matsudaira, P. (2000). Motility powered by supramolecular springs and ratchets. *Science* **288**, 95–100.
- Gogendeau, D., Klotz, C., Arnaiz, O., Malinowska, A., Dadlez, M., de Loubresse, N.G., Ruiz, F., Koll, F., and Beisson, J. (2008). Functional diversification of centrins and cell morphological complexity. *J. Cell Sci.* **121**, 65–74.
- Allen, R.D. (1973). Contractility and its control in peritrich ciliates. *J. Protozool.* **20**, 25–36.
- Bannister, L.H., and Tatchell, E.C. (1968). Contractility and the fibre systems of *Stentor coeruleus*. *J. Cell Sci.* **3**, 295–308.
- Pearson, C.G., and Winey, M. (2009). Basal body assembly in ciliates: the power of numbers. *Traffic* **10**, 461–471.
- Marshall, W.F. (2011). Origins of cellular geometry. *BMC Biol.* **9**, 57.
- Jennings, H.S. (1899). The mechanism of the motor reactions of *Paramecium*. *Am. J. Physiol.* **2**, <https://doi.org/10.1152/ajplegacy.1899.2.4.311>.
- Naitoh, Y., and Eckert, R. (1969). Ionic Mechanisms Controlling Behavioral Responses of *Paramecium* to Mechanical Stimulation. *Science* **164**, 963–965.
- Kung, C., and Saimi, Y. (1982). The physiological basis of taxes in paramecium. *Annu. Rev. Physiol.* **44**, 519–534.
- Amos, W.B. (1971). Reversible mechanochemical cycle in the contraction of *Vorticella*. *Nature* **229**, 127–128.
- Upadhyaya, A., Baraban, M., Wong, J., Matsudaira, P., van Oudenaarden, A., and Mahadevan, L. (2008). Power-limited contraction dynamics of *Vorticella convallaria*: an ultrafast biological spring. *Biophys. J.* **94**, 265–272.
- Osborn, D., Hsung, J.C., and Eisenstein, E.M. (1973). The involvement of calcium in contractility in the ciliated protozoan, *Spirostomum ambiguum*. *Behav. Biol.* **8**, 665–677.
- Mathijssen, A.J.T.M., Culver, J., Bhamla, M.S., and Prakash, M. (2019). Collective intercellular communication through ultra-fast hydrodynamic trigger waves. *Nature* **571**, 560–564.
- Miller, S. (1968). The Predatory Behavior of *Dileptus anser* *. *J. Protozool.* **15**, 313–319.
- Visscher, J.P. (1927). A neuromotor apparatus in the ciliate *Dileptus gigas*. *J. Morphol.* **44**, 373–381.
- Ricci, N., and Verni, F. (1988). Motor and predatory behavior of *Litonotus lamella* (Protozoa, Ciliata). *Can. J. Zool.* **66**, 1973–1981.
- Mast, S.O. (1911). Habits and reactions of the ciliate *Lacrymaria*. *J. Anim. Behav.* **1**, 229–243.
- Bohatier, J. (1970). Structure et ultrastructure de *Lacrymaria olor*(O.F.M. 1786). *Protistologica (Paris)* **6**, 331–342.
- Bradske, G., and Kaehler, A. (2000). OpenCV. Dr. Dobb's J. Softw. Tools **3**.
- Zivkovic, Z. (2004). Improved adaptive Gaussian mixture model for background subtraction. In *Proceedings of the 17th International Conference on Pattern Recognition. ICPR 2004/Vol. 2 (IEEE)*, pp. 28–31.
- Purcell, E.M. (1977). Life at low Reynolds number. *Am. J. Physiol.* **45**, 3–11.
- Tatchell, E.C. (1981). An ultrastructural study of prey capture and ingestion in *lacrymaria olor*. *Protistologica* **17**, 59–66.
- Yanase, R., Nishigami, Y., Ichikawa, M., Yoshihisa, T., and Sonobe, S. (2018). The neck deformation of *Lacrymaria olor* depending upon cell states. *J. Protistol.* **51**, 1–6.

39. Maloney, M.S., McDaniel, W.S., Locknar, S.A., and Torgina, H.M. (2005). Identification and localization of a protein immunologically related to Caltractin (Centrin) in the Myonemes and Membranelles of the Heterotrich ciliate Stentor coeruleus. *J. Eukaryot. Microbiol.* 52, 328–338.
40. Truesdell, C.A. (1960). The Rational Mechanics of Flexible or Elastic Bodies: 1638–1788: Introduction to Leonhardi Euleri Opera Omnia/vol. 10. et 11., Seriei Secundae (Auctoritate et impensis Societatis scientiarum naturalium Helveticae).
41. Stephens, G.J., Johnson-Kerner, B., Bialek, W., and Ryu, W.S. (2008). Dimensionality and dynamics in the behavior of *C. elegans*. *PLoS Comput. Biol.* 4, e1000028.
42. Plattner, H., and Klauke, N. (2001). Calcium in ciliated protozoa: sources, regulation, and calcium-regulated cell functions. *Int. Rev. Cytol.* 201, 115–208.
43. Noguchi, M., Nakamura, Y., and Okamoto, K.I. (1991). Control of ciliary orientation in ciliated sheets from Paramecium—differential distribution of sensitivity to cyclic nucleotides. *Cell Motil. Cytoskeleton* 20, 38–46.
44. Winegar, B.D., Kelly, R., and Lansman, J.B. (1991). Block of current through single calcium channels by Fe, Co, and Ni. Location of the transition metal binding site in the pore. *J. Gen. Physiol.* 97, 351–367.
45. Perry, G. (1999). The Evolution of Search Modes: Ecological versus Phylogenetic Perspectives. *Am. Nat.* 153, 98–109.
46. Viswanathan, G.M., Buldyrev, S.V., Havlin, S., da Luz, M.G.E., Raposo, E.P., and Stanley, H.E. (1999). Optimizing the success of random searches. *Nature* 401, 911–914.
47. Bell, W.J. (1990). Searching Behaviour: The Behavioural Ecology of Finding Resources (Springer Netherlands).
48. Kramer, D.L. (2001). Foraging behavior. In *Evolutionary Ecology: Concepts and Case Studies*, C.W. Fox, D.A. Roff, and D.J. Fairbairn, eds. (Oxford University Press), pp. 232–246.
49. Pyke, G.H., Pulliam, H.R., and Charnov, E.L. (1977). Optimal Foraging: A Selective Review of Theory and Tests. *Q. Rev. Biol.* 52, 137–154.
50. Turner, L., Ryu, W.S., and Berg, H.C. (2000). Real-time imaging of fluorescent flagellar filaments. *J. Bacteriol.* 182, 2793–2801.
51. Jikeli, J.F., Alvarez, L., Friedrich, B.M., Wilson, L.G., Pascal, R., Colin, R., Pichlo, M., Rennhack, A., Brenker, C., and Kaupp, U.B. (2015). Sperm navigation along helical paths in 3D chemoattractant landscapes. *Nat. Commun.* 6, 7985.
52. Weiner, O.D., Servant, G., Welch, M.D., Mitchison, T.J., Sedat, J.W., and Bourne, H.R. (1999). Spatial control of actin polymerization during neutrophil chemotaxis. *Nat. Cell Biol.* 1, 75–81.
53. Beisson, J., Betermier, M., Bre, M.H., Cohen, J., Duhamel, S., Duret, L., Kung, C., Malinsky, S., Meyer, E., Preer, J.R., et al. (2010). Immunocytochemistry of Paramecium Cytoskeletal Structures. *Cold Spring Harb. Protoc.* 2010, pdb.prot5365.
54. Korobchevskaya, K., Lagerholm, B., Colin-York, H., Fritzsche, M., Korobchevskaya, K., Lagerholm, B.C., Colin-York, H., and Fritzsche, M. (2017). Exploring the Potential of Airyscan Microscopy for Live Cell Imaging. *Photonics* 4, 41.
55. Gilpin, W., Prakash, V.N., and Prakash, M. (2017). Flowtrace: simple visualization of coherent structures in biological fluid flows. *J. Exp. Biol.* 220, 3411–3418.

STAR★METHODS

KEY RESOURCES TABLE

REAGENT or RESOURCE	SOURCE	IDENTIFIER
Antibodies		
Alexa Fluor 488 conjugated anti-alpha-tubulin antibody	Invitrogen	RRID: AB_2532182
Anti-centrin mouse monoclonal antibody	Millipore	RRID: AB_10563501
Alexa Fluor 568 conjugated anti-mouse IgG antibody	Invitrogen	RRID: AB_2534072
Chemicals, Peptides, and Recombinant Proteins		
1% Knop's Solution	Ward's Science	470301-800
Experimental Models: Cell Lines		
Lacrymaria olor	This paper (originally from Ryuji Yanase)	N/A
Cyclidium sp.	This paper (originally from Ryuji Yanase)	N/A
Software and Algorithms		
Segmentation, tracking, analysis and modeling scripts	This paper	https://github.com/scoyle79/LacrymariaBehavior
Other		
Single cell behavioral tracks	This paper	https://github.com/scoyle79/LacrymariaBehavior

LEAD CONTACT AND MATERIALS AVAILABILITY

Further information and requests for *Lacrymaria* cells or their *Cyclidium* prey, resources and reagents should be directed to and will be fulfilled by the Lead Contact, Manu Prakash (manup@stanford.edu). This study did not generate new unique reagents.

EXPERIMENTAL MODEL AND SUBJECT DETAILS

Cell lines

Lacrymaria was cultured in 200 mL of 0.01% Knop's solution in T225 tissue culture flasks. Each culture was fed 100 mL of concentrated and washed *Cyclidium* prey twice a week. *Cyclidium* was cultured in 250 mL 0.01% Knops over 25 mL of an agar nutritional pad in a 300 mL Erlenmeyer flask. Additional details for culturing both cell lines are outlined in the Method Details.

METHOD DETAILS

Detailed culture methods

The field isolates of *Lacrymaria olor* that provided us with our initial behavioral observations were originally obtained from the Palo Alto Duck Pond (37.4571° N, 122.1088° W). The large-scale cultures needed for quantitative behavioral studies were grown using a *Lacrymaria* starter culture and *Cyclidium* prey culture characterized by Ryuji Yanase of Hyogo University, Japan. Cultures were grown using methods developed by Yanase [38], with modification to significantly increase densities and facilitate long-term behavioral imaging of small-scale cultures that we describe here. A graphic depicting the culturing process is included in Figure S7.

Cyclidium was grow using 0.01% Knop's solution as the liquid medium (Flinn Scientific). Low maintenance “time-release” cultures were grown in darkness in 250 mL 0.01% Knop's on top of a 25 mL nutritional agar pad (2% Agar, 1 mg/ml Yeast Extract, 1 mg/ml Skim Milk). These cultures support a modest density of *Cyclidium* for 2–3 weeks. To improve *Cyclidium* yields for feeding to *Lacrymaria*, the contents of a 250 mL flask were transferred to 8x160mm Petri dishes and expanded in the dark for 3 days. These high-density cultures were pooled and 2.5 mL of this culture was used to start new 250 mL cultures at a 1:100 dilution.

To feed *Cyclidium* preys to *Lacrymaria*, 250 mL of expanded *Cyclidium* culture was passed through a 70 µm filter and the filtrate subsequently passed through a 40 µm filter (Pluriselect). The filtered cells were harvested by centrifugation at 500xRCF, and washed twice with one culture volume of fresh 0.01% Knop's. The resulting pellet was resuspended in 100 mL 0.01% Knop's and provided enough food to sustain 4x250mL *Lacrymaria* cultures for 3–4 days.

Lacrymaria cultures were grown in T225 TC-treated tissue culture flasks (Corning). We found that TC-treatment improved attachment of *Lacrymaria* in large-scale cultures and facilitated expansion and growth. *Lacrymaria* were grown in a standing volume of 200 mL 0.01% Knop's in the dark. Nutrition was provided exclusively in the form of concentrated and cleaned prey foods to prevent

excess bacterial growth and maintain homogeneous culture conditions. *Lacrymaria* were fed 250 mL washed and cleaned *Cyclidium* per 1000 mL of *Lacrymaria* culture twice a week.

After feeding, 25–50 mL of *Lacrymaria* culture was removed and the cells were concentrated at 500×RCF for 5 minutes and resuspended in 1/20 volume of 0.01% Knop's. 100–200 μ L aliquots of the resulting cell-suspension were dispensed into the wells of a 96-well Corning imaging plate. This centrifugation initially disrupts *Lacrymaria* morphology, however within 24 hours most cells have repaired any damage to their necks, attached to the culture plate and begin performing regular hunting events. *Lacrymaria* subcultures grown in these plates could persist for 1–2 weeks, depending on the initial density of prey in the culture.

As the natural ecosystem of these plates depends on small bits of agar and detritus to support the base of the food chain, these subcultures were often too dirty for certain imaging applications. When cleaner cultures were required, for example for high contrast dark-field imaging, cells were carefully pipetted out of one microwell and transferred to a clean one, leaving most of the sticky particulate matter, agar, and detritus behind on the bottom of the well. These cleaned subcultures could typically grow for 2–3 days before exhausting.

Immunostaining and Confocal imaging

Immunostaining was performed as for other ciliates with modification to better preserve three-dimensional structure and neck shape [38, 53]. Briefly, cells were grown in 96-well plates in 100 μ L volumes of Knop's media overnight and fixed for 30 minutes directly in the well by addition of 100 μ L of fixative solution (2% (w/v) PFA and 0.5% (w/v) Triton X-100 in PHEM buffer). The top 100 μ L of the fixative solution was then removed and replaced with 0.05 M glycine in PBS. The cells were left in this solution for 20 minutes then treated with blocking solution (0.2% bovine serum albumin (w/v) in PBS) for 30 minutes. The cells were then incubated in antibody solution (0.1% (w/v) BSA, 0.1% (w/v) Triton X-100 in PBS) containing a 1:500 dilution of anti-centrin mouse monoclonal antibody (Millipore, 04-1624) for 1 hour. The cells then were washed 3 times for 10 minutes in PBS containing 0.2% (w/v) Triton X-100 and left incubating in Alexa Fluor 568 conjugated anti-mouse IgG antibody (Invitrogen) diluted 1:1000 in the antibody solution for an hour. Cells were again washed 3 times for 10 minutes and left incubating in antibody solution containing the Alexa Fluor 488 conjugated anti-alpha-tubulin antibody (Invitrogen) diluted 1:500 for 1 hour. The cells were washed 3 more times and then mounted onto glass slides. Images were collected using either an LSM 780 or LSM 880 microscope using the airy-scan technique [54] where indicated.

High-speed imaging

High-speed imaging of head and neck cilia was performed using a 40x DIC Objective (Nikon) and a Phantom high-speed camera. Cells were sealed between a slide and coverslip using 2 pieces of double-sided tape as a spacer. Confinement was necessary to effectively resolve cilia with the high-speed camera. Although cells confined in this way had reduced mobility and extension compared to cells grown in unconfined cultures, cells still performed repeated extension and retraction of their necks. Data were acquired at 1000 frames per second using the associated Phantom software, and the resulting files were converted into ordinary AVI files for inspection and analysis.

Flow-trace imaging of tracer particles

Cells from a dense 100 μ L subculture were transferred to a clean 24-well 18mm inset glass-bottom imaging plate (Makitek). 5 μ m beads fluorescent or non-fluorescent beads (Polysciences) were added to the solution. For low-mag visualization of flows (Video S2), the motion of particles was visualized using Flash-Red fluorescent beads (Polysciences). For high-mag visualization of flows, the motion of particles was determined using 5 μ m non-fluorescent beads (Polysciences) and a 40x DIC objective (Nikon). Because the cell morphology changes during extension and retraction it is difficult to coherently analyze every class of flow produced by the cell. However, the head generates very strong flows, particularly when it is fully extended, and these flows can be recognized as a stokeslet flow when the resulting images are analyzed using FlowTrace [55].

Darkfield timelapse imaging

Cells from a dense 100 μ L subculture were transferred to a clean 24-well 18mm inset glass-bottom imaging plate (Makitek) or 96-well polycarbonate bottom imaging plate (Corning). The well was covered with a coverslip and sealed with VALAP to prevent evaporation. After 24 hours, the cells had reattached the plate surface and were ready for timelapse imaging. Timelapse darkfield imaging for morphology tracking and segmentation was captured with an inverted scope (Nikon) with a 2x objective (Nikon) and ring illumination; or a custom-built imaging setup using a Leopard IMX-274 MIPI-CS camera (Leopard Imaging), non-inverted 2x objective (Mitutoyo), ring LED-illumination, and encoded into 4K H264 video using an Nvidia Jetson GPU (see Figure S7). The latter setup facilitates collecting extremely long behavioral video that is suitable for analysis but also readily shareable with the scientific community and general public (available at the CiliateWorld YouTube channel).

Image processing, segmentation, tracking, and data processing and modeling

Our analysis of cellular behavior from timelapse darkfield video was performed using custom python scripts that take advantage of the OpenCV computer vision package [34]. The source code is available at the GitHub page associated with this paper (<https://github.com/scoyle79/LacrymariaBehavior>), and we describe here the general approach used in our tracking of subcellular posture. Because the cell morphology of *Lacrymaria* (fat body, thin neck, motile head) contains multiple visually distinct elements, we found no single thresholding or filtering method could consistently segment *Lacrymaria* cells. Instead, we created a composite segmentation

based on using filters that recognize different aspects of its subcellular anatomy: a dynamic MOG background subtractor to identify the small but highly motile head structure [35]; a very stringent simple threshold to locate the extremely bright bodies of *Lacrymaria* cells; and a canny-edge detector that was effective at identifying the neck that connects the two. Cells were identified from this composite segmentation by first defining them in terms of a body, and then locating the associated head and neck. Tracking of single cells was performed using this composite segmentation, and different features of subcellular anatomy and their relative positions to one another were used to orient the geometry of the organism. The resulting tracks contain all information necessary to reconstruct the complete shape, geometry, position, and morphology of cells during the timelapse (see [Video S2](#)). To align data for the same cell to a fixed body position and orientation, the centroid of the body and its tail-to-neck-junction angle were extracted and used to translate and rotate all points in our spline to a common orientation.

Our analysis of *Lacrymaria* shapes using principal component analysis was performed using a method previously used to characterize the locomotory behavior of *C. elegans* [41]. Briefly, each neck shape was fit with a spline of 100 points, the tangent angle at each point $\theta(s)$ was calculated, and the resulting description was normalized such that the mean $\theta(s)$ is 0. The resulting set of neck shapes ($> 100,000$ per cell) is coordinate-free and length-independent, which allows the PCA-derived shapes we generate to be used to explore trends with other independent parameters in the system like length. The covariance matrix for the shapes was calculated and the associated eigenvectors and eigenvalues determined using the Numpy package in python. Fits of observed neck data to the first four eigenshapes was performed by least-squares fitting. Qualitative comparison (mode scaling and length scaling) to a simple elastic filament was based on the textbook buckling equations derived from classical beam theory, reproduced in [Figure 5A](#) and [Figure S4](#) [40].

The simulated sampling areas in [Figure 7B](#) were produced using a python code that can be found on our paper's associated GitHub. Briefly, because buckling occurs when $L_{\text{obs}} < L_0$, extensile trajectories are repeatedly sampled from the location L_0 by (1) drawing a shape from our empirical shape distributions and using its associated tip angle for extension and (2) drawing an extension length from our length distributions we measured associated with L_0 . The value of L_0 throughout the sampling can be set by an arbitrary function to model the slow dynamics of neck extension and retraction. The empirical shape and length distributions can also be replaced with any distribution or function of the modelers choosing – as was done to produce the plots in [Figure S6](#).

Perturbation experiments

Perturbation experiments were performed by exchanging the media in a well with 0.01% Knop's media containing the perturbant at the indicated concentration. The particular perturbations described in this study target fast timescale signaling controllers and produced phenotypes within seconds upon addition. The specific perturbations we performed were 0.01% Knop's + 5 mM CaCl₂, 0.01% Knop's + 10 mM EGTA, and 0.01% Knop's + 1 mM CoCl₂.

QUANTIFICATION AND STATISTICAL ANALYSIS

Statistical details of the experiments can be found in the figure legends, figures themselves, the text, or the Method Details section of the [STAR Methods](#). Statistical details include exact value of n, what n represents (typically the number of morphologies measured, the number of cells measured, or the number of hunting events measured), definitions of center, and dispersion and precision measures. Statistical fits were performed as described in the Method Details section using Numpy packages in Python and the analysis codes are available on our associated GitHub repository.

DATA AND CODE AVAILABILITY

The image processing, tracking, and analysis, and modeling python code is available on our associated GitHub Repository. The single-cell timeseries tracks used in this study will be available as a Pickled data file through a link on our GitHub, which can be opened in Python and analyzed using any analysis pipeline of one's choosing.